PAPER

Improved self-powered perovskite CH₃NH₃PbI₃/SnO₂ heterojunction photodetectors achieved by interfacial engineering with a synergic effect

Guipeng Li,[a] Huimin Zhang,[a] Weihao Qin[b] and Mingming Chen [ID] *[a]

Lead halide perovskite heterojunctions have been considered as important building blocks for fabricating high-performance photodetectors (PDs). However, the interfacial defects induced non-radiative recombination and interfacial energy-level misalignment induced ineffective carrier transport severely limit the performance of photodetection of resulting devices. Herein, interfacial engineering with a spin-coating procedure has been studied to improve the photodetection performance of CH₃NH₃PbI₃/SnO₂ heterojunction PDs, which were fabricated by sputtering a SnO₂ thin film on ITO glass followed by spin-coating a CH₃NH₃PbI₃ thin film. It has shown that spin-coating of a SnO₂ layer on the sputtered SnO₂ thin films suppressed the surface oxygen vacancies of SnO₂ thin films and up-shifted their conduction band, which suppressed the interfacial non-radiative recombination and enhanced the carriers transport at the CH₃NH₃PbI₃/SnO₂ interface, respectively. Accordingly, improved photodetection performance, such as the reduced dark current and increased photocurrent, has been observed in the CH₃NH₃PbI₃/SnO₂ heterojunction PDs, where the responsivity and detectivity of 0.077 A W⁻¹ and 2.0 × 10¹¹ jones, respectively, at the zero bias have been demonstrated. These results show a simple way to suppress the interfacial non-radiative recombination and enhance the carrier transport at the interface to fabricate improved perovskite heterojunction PDs in the future.

Introduction

Photodetectors (PDs), which convert photons into electric charge, have attracted much attention recently owing to their important applications in various areas including digital imaging, optical communications, medical analysis, and environment monitoring.[1–4] In general, PDs can be classified into two categories, *i.e.*, photoconductors and photodiodes. The former ones possess a simple device structure but feature a high noise current and low photoconductive gains.[5] In contrast, the latter ones have usually been characterized with a low noise current and high photon-to-electric conversion efficiencies owing to the presence of an interfacial barrier and a strong built-in electric field.[6,7] Additionally, the photodiodes can operate without the requirement of a power supply. Heterojunctions, which are composed of two different semiconductors bound together, have been considered as important building blocks for photodiodes owing to simple fabrication process regarding free-of-controlled n- and p-type doping of selected semiconductors. In recent years, lead halide perovskites (LHPs) with a formula of ABX₃ (where A is the CH₃NH₃⁺ (MA⁺), and

HC(NH₂)₂⁺ (FA⁺); B is the Pb²⁻; X is the Cl⁻, Br⁻, and I⁻) have attracted much attention from the optoelectronics community due to their outstanding properties such as long charge carriers lifetime, long charge carriers diffusion length, high absorption coefficient, widely tunable energy bandgap, and low-temperature solution processability.[8] Benefiting from these advantages, LHP heterojunctions have been considered as promising candidates for achieving efficient photodetection.[9–12]

Generally, the working principles of PDs are similar to those of solar cells (SCs), where excess carriers are generated due to the valance-band-to-conduction-band transition upon light illumination, followed by the collection of excess carriers by the electrodes. As a wide bandgap semiconductor, tin dioxide (SnO₂) features a high electron mobility, deep conduction band, and low-temperature processability, and has widely been employed as an electron transport layer to fabricate efficient SCs recently.[13–15] Meanwhile, various PDs have recently been demonstrated based on LHP/SnO₂ heterojunctions.[16–18] Similar to LHP SCs, the performance of LHP PDs is mainly related to the collection efficiencies of excess carriers, which are limited by the trap-assisted non-radiative recombination and ineffective carrier transport.[19] In heterojunction PDs, the former is mainly related to the bulk and interfacial defects, while the latter is owing to the energy-level misalignment at the heterojunction interface. Notably, various strategies have been explored to improve the crystalline quality of LHP thin films recently, which

[a]Department of Microelectronics, Jiangsu University, Zhenjiang, Jiangsu 212013, China. E-mail: andychain@live.cn

[b]School of Materials Science and Engineering, East China University of Science and Technology, Shanghai, 200237, China

facilitated the rapid development of power conversion efficiency (PCE) of LHP SCs.[20] Typically, doping of elements has resulted in an increase in grain sizes and a suppression of intrinsic defects (such as halide and Pb vacancies) in LHP thin films and nanocrystals.[21] Besides, interfacial engineering with a thin dielectric layer and anchoring groups have been demonstrated but primarily to suppress the interfacial non-radiative recombination.[22] In contrast, the alignment of energy-level at the heterojunction interface has seldom been explored before. Practically, both interfacial passivation and energy-level alignment are fundamental for fabricating high-performance heterojunction PDs.[23] Herein, we showed the fabrication of improved solution-processed $MAPbI_3/SnO_2$ heterojunction PDs by employing a stacked SnO_2 thin film prepared by sputtering and spin-coating methods in sequence. It showed that the subsequent spin-coating procedure behaved a synergic effect including a suppression of interfacial defects and alignment of the energy-level at the $MAPbI_3/SnO_2$ interface. Accordingly, a decreased dark current and an increased photocurrent have been demonstrated simultaneously in the $MAPbI_3/SnO_2$ heterojunction PDs. Finally, improved performance of photodetection with the responsivity and detectivity as high as 0.077 A W^{-1} and 2×10^{11} jones, respectively, at the zero bias have been evidenced.

Experiments

$MAPbI_3/SnO_2$ heterojunctions (Fig. 1b) were fabricated by spin-coating a $MAPbI_3$ thin film onto a stacked SnO_2 thin film, which was prepared by sputtering a SnO_2 thin film on cleaned ITO glasses then followed by spin-coating a thin SnO_2 layer. In detail, the ITO glasses were cleaned with acetone, ethanol and DI water in sequence. After that, a thin SnO_2 film was firstly grown using a sputtering method with a growth temperature of 500 °C and growth time of 10 min (labeled as SnO_2-1). The RF power is 80 W. The Sn source was provided by a SnO_2 target (99.99%). Ar/O_2 with a flow of 55 sccm/5 sccm were used as working gas. Then, a thin SnO_2 layer was grown by spin-coating to obtain the stacked SnO_2 thin films (labeled as SnO_2-2), in which the SnO_2 precursor solution (3 wt%) was prepared by diluting SnO_2 nanoparticles (~20 nm) into DI water. Finally, $MAPbI_3$ thin films were grown on SnO_2-2 (labeled as $MAPbI_3$-2) according to previous reports.[24] The perovskite precursor was prepared by dissolving PbI_2 and MAI into DMF/GBL/DMSO mixtures. The perovskite precursor was spin-coated with a two-step program (1000 rpm for 10 s and 5000 rpm for 20 s), where 400 μL toluene was dropped at 8 s of the second program. To reveal the roles of the spin-coated SnO_2 thin layer, $MAPbI_3$ thin films were directly prepared onto SnO_2-1 (labeled as $MAPbI_3$-1), as shown in Fig. 1a. The PDs were obtained by depositing a thin Au electrode with an area of 0.01 mm^2 on the $MAPbI_3$ thin films and an Ag paste on ITO.

The morphology and structure of SnO_2 and $MAPbI_3$ thin films were studied by field-emission scanning electron microscopy (SEM, JSM-7800F) and X-ray diffraction (XRD, Bruker D8 with Cu Kα radiation of 1.54 Å). The steady-state photoluminescence (PL) spectra of $MAPbI_3$ thin films were obtained

with the excitation of a cw 405 nm laser. The power of the incident laser was modulated by an attenuator. The transient PL spectra were excited with a ps-pulse laser at 450 nm, and the data were recorded by a ps time-correlated single photon counting technique. The absorption spectra were collected on an ultraviolet-visible spectrophotometer. The atomic electron binding energies of SnO_2 thin films were studied by X-ray photoelectron spectroscopy (XPS). The work function and energy band structure of SnO_2 were studied by ultraviolet photoelectron spectroscopy technique (UPS) using He I as the excitation source.

The performance of $MAPbI_3/SnO_2$ heterojunction PDs was studied by a photoresponse system consisting of a Xe lamp, a monochromator, an electronic shutter, two probers, a microscope, a Keithley 2401 source-measure unit (SMU), and a semiconductor parameter analyzer (Keysight, B1500A). All experiments were carried out in the atmosphere with a humidity of ~55–60%.

Results and discussions

Fig. 1c and d exhibit the SEM images of SnO_2-1 and SnO_2-2 thin films. It can be seen that the SnO_2-1 thin films feature a smooth surface (Fig. 1c). This can be attributed to the high growth temperature (500 °C, as mentioned above), which facilitated the migration of species at the substrate surface. In comparison, a rough surface has been observed in the SnO_2-2 thin films (Fig. 1d). According to previous report,[25] a rough surface of buried layer increases the contact area at the $MAPbI_3/SnO_2$ interface, which improves the optical absorption in the $MAPbI_3$ thin films. XRD were carried out to investigate the crystalline structures of SnO_2-1 and SnO_2-2 thin films, and the results are illustrated in Fig. 1i. As depicted, both the SnO_2 thin films exhibit a similar crystalline structure. According to the XRD peaks which are located at 22.3°, 33.5°, 36.8°, and 52.5°, both the SnO_2 thin films were crystallized into tetragonal with a space group of $P4_2/mnm$.

Fig. 1e and f exhibit the SEM images of $MAPbI_3$ thin films grown on SnO_2-1 and SnO_2-2. It shows that both the $MAPbI_3$ thin films have a dense structure, which is fundamental for the subsequent fabrication of heterojunction PDs. Notably, the grain sizes of $MAPbI_3$ thin films grown on SnO_2-2 are around 200 nm, which is slightly larger than those grown on SnO_2-1 (150 nm). In general, the $MAPbI_3$ thin films with a larger grain size possess a decreased density of boundary defects, which is favorable to improve the photodetection performance of resulting PDs.[26,27]

Fig. 1j shows the XRD patterns of $MAPbI_3$ thin films grown on SnO_2-1 and SnO_2-2. It shows that both the $MAPbI_3$ thin films exhibit a similar crystalline structure and quality. Accordingly, the spin-coated SnO_2 layer did not affect the growth of $MAPbI_3$ thin films. Further observations show that the contact angle of SnO_2-2 is comparable to that of SnO_2-1 (Fig. 1g and h), which is responsible for the similar crystalline quality of the two $MAPbI_3$ thin films.

As mentioned above, the SnO_2-2 thin films were grown by sputtering and spin-coating SnO_2 layers in sequence. In the
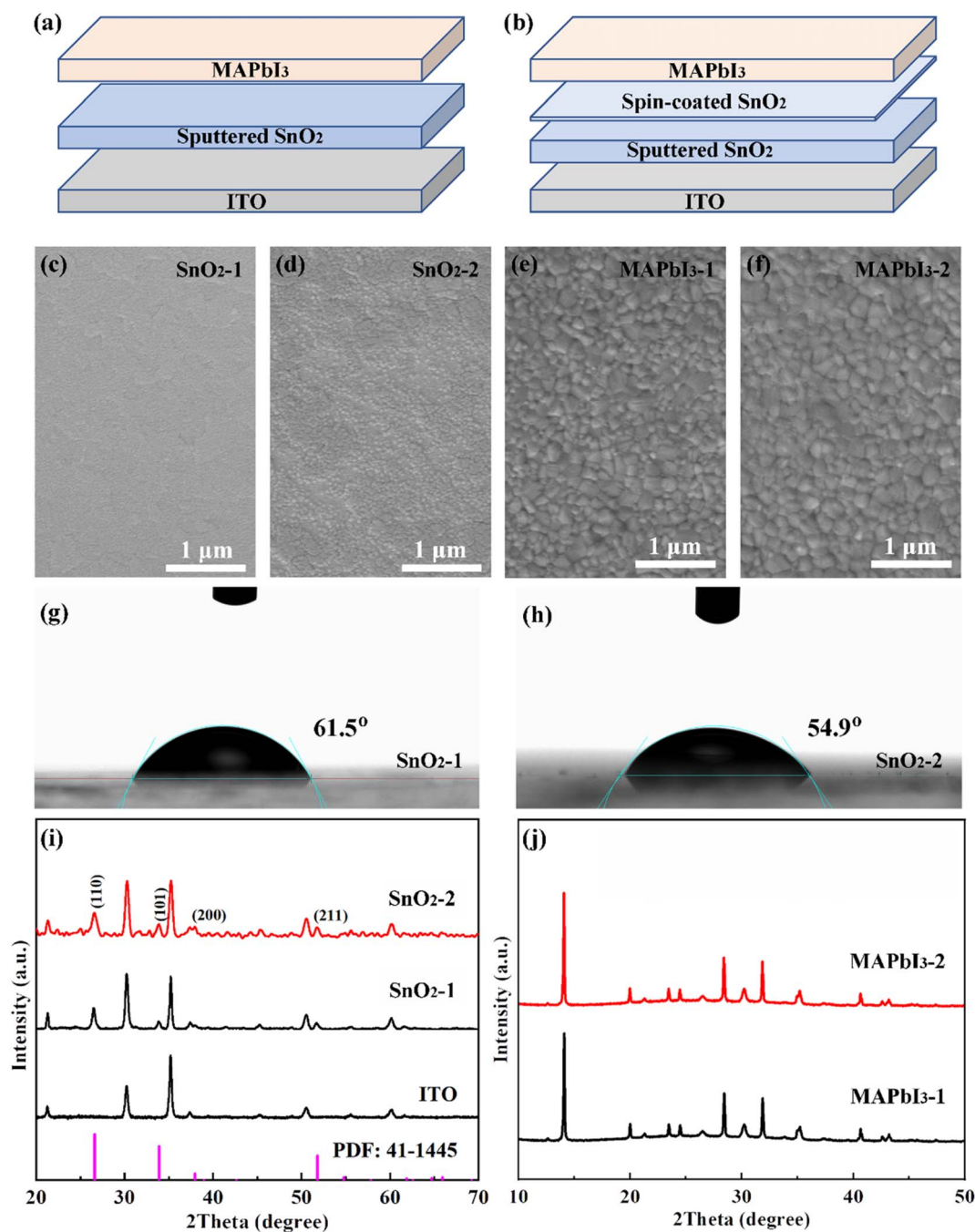
Fig. 1 Characteristics of SnO$_2$ and MAPbI$_3$ thin films. (a and b) Scheme of MAPbI$_3$/SnO$_2$-1 and MAPbI$_3$/SnO$_2$-2 heterojunctions. (c−f) SEM images of SnO$_2$ and MAPbI$_3$ thin films. (g and h) Water contact angles of SnO$_2$ thin films. (i and j) XRD patterns of SnO$_2$ and MAPbI$_3$ thin films.

latter case, the SnO$_2$ precursor was prepared by diluting the SnO$_2$ nanoparticles in DI water, therefore oxhydryl groups (OH$^-$) tended to be doped into the SnO$_2$ thin films.[28] To verify this, XPS measurements were performed, and the results are shown in Fig. 2. As depicted in Fig. 2a, only Sn and O signals were observed in both the SnO$_2$ thin films. This suggests that no impurities were incorporated during the preparation processes. Fig. 2b exhibits the O 1s core-level spectra of SnO$_2$-1 and SnO$_2$-2. The binding energies are observed at around 530.5 eV, 531.3 eV, and 532.5 eV, which are associated with Sn–O, oxygen vacancies

(V$_O$), and OH$^-$, respectively.[29] As reported, the content of various components can be qualitatively evaluated from their intensities of XPS peaks.[29] Accordingly, the SnO$_2$-2 shows an increased content of OH$^-$ and a reduced content of V$_O$ compared to SnO$_2$-1. The former is related to the oxhydryl groups in the aqueous solution. The reasons for latter are unclear currently, but should be related to the SnO$_2$ nanoparticles used. Importantly, it has reported that surface treatment with oxhydryl groups tuned the energy band of buried layers.[30] As shown later, the SnO$_2$-2 thin films show an increased conduction band, which aligned the
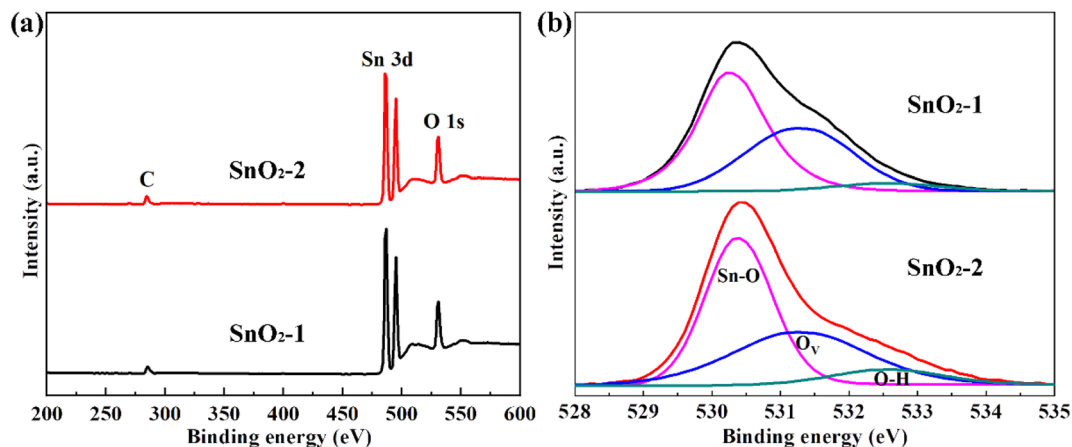
Fig. 2 XPS curves of SnO$_2$ thin films. (a) XPS survey spectra. (b) O 1s core-level spectra.

energy-level at the MAPbI$_3$/SnO$_2$ interface. Meanwhile, the reduced V$_O$ suppressed the non-radiative recombination at the MAPbI$_3$/SnO$_2$ interface.[31]

Fig. 3 shows the steady-state and time-resolved PL spectra of MAPbI$_3$ thin films grown on SnO$_2$-1 and SnO$_2$-2. It can be seen that the PL spectra captured from the front surface of MAPbI$_3$ thin films exhibit similar intensity and lifetime (Fig. 3a and c), showing that both MAPbI$_3$ thin films possess similar crystalline quality. This is in consistence with the XRD and SEM results shown above. Notably, the PL spectra captured from the back surface of MAPbI$_3$ thin films exhibit distinct behaviors. As can be seen in Fig. 3b and d, the MAPbI$_3$ thin films prepared on SnO$_2$-2 exhibit a decreased PL intensity and lifetime. This suggests that the spin-coated SnO$_2$ layer enhanced the extraction of electrons at the MAPbI$_3$/SnO$_2$ interface. Similar phenomena have been reported in graphdiyne decorated MAPbI$_3$/SnO$_2$ and Mg^{2+} decorated MAPbI$_3$/NiO heterojunctions.[32–34] As shown below, the slight up-shift of the conduction band of the SnO$_2$-2 thin films aligned the interfacial energy-level, which is responsible for the decreased PL intensity and lifetime in the back surface of MAPbI$_3$/SnO$_2$-2 heterojunctions.

Additionally, the interfacial defects at the MAPbI$_3$/SnO$_2$ interfaces were further studied from the excitation power dependent integrated PL, and the results are shown in Fig. 3e and f. As depicted in Fig. 3e, the PL spectra of both MAPbI$_3$ thin films exhibit similar patterns with an increase in excitation power, showing that the recombination processes of excess carriers kept unchanged. Fig. 3f depicts the relationship between integrated PL intensity and corresponding excitation power. According to the trap-filling model, the PL intensity increases slowly with an increase in excitation power under the low excitation level, while it increases rapidly with the excitation power under the high excitation level.[17,35,36] As a result, the density of trap states (n_{trap}) is proportional to the excitation power threshold of complete trap filling (P_{th}), i.e., $n_{trap} \propto P_{th}$.[17,35,36] As shown in Fig. 3f, the P_{th} for MAPbI$_3$ grown on SnO$_2$-1 and SnO$_2$-2 were observed at 9.2 μW and 10.9 μW, respectively. This suggests that around 10% trap states have been reduced at the MAPbI$_3$/SnO$_2$-2 interface compared to MAPbI$_3$/SnO$_2$-1

interface. It is speculated that the reduced trap states at the MAPbI$_3$/SnO$_2$-2 interface is associated with the decreased surface V$_O$ of the SnO$_2$-2 thin films as verified from XPS results shown above.

The energy band structure of SnO$_2$ thin films was further studied by UPS and UV-vis absorption results. Fig. 4 exhibits the UPS spectra of SnO$_2$-1 and SnO$_2$-2 thin films. As reported before, the valence band maximum (E_V) can be calculated from the following eqn (1):[37]

$$E_V = -[h\nu - (E_{cutoff} - E_V^F)] \qquad (1)$$

where $h\nu$ is the photon energy of He I lamp (21.22 eV), E_{cutoff} is the cutoff energy of the secondary electrons, and E_V^F is the injection barrier (schematically shown in Fig. 4a). As shown in Fig. 4a and b, the E_{cutoff} are 16.31 eV and 16.20 eV, and the E_V^F are 3.41 eV and 3.17 eV for SnO$_2$-1 and SnO$_2$-2, respectively. This results in the E_V as −8.32 eV and −8.19 eV accordingly. In addition, according to the UV-vis absorption spectra shown in Fig. 4c and d, where the optical bandgap of SnO$_2$-1 and SnO$_2$-2 were obtained as around 4.1 eV, the corresponding conduction band minimums (E_C) were calculated as −4.19 eV and −4.02 eV. This demonstrates that the spin-coating procedure up-shifted the conduction band (+0.13 eV) of the SnO$_2$ thin films. Similar phenomena have been demonstrated in graphdiyne and NH$_4$S decorated SnO$_2$ thin films reported before.[33,38,39] Accordingly, the energy band diagrams of SnO$_2$-1 and SnO$_2$-2 thin films were obtained, as shown in Fig. 4a and b inset.

After depositing thin circular Au electrodes on MAPbI$_3$ thin films and Ag paste on ITO, MAPbI$_3$/SnO$_2$ heterojunction PDs were fabricated. Fig. 5a illustrates the current–voltage (I–V) curves of MAPbI$_3$/SnO$_2$-1 and MAPbI$_3$/SnO$_2$-2 PDs captured in dark and under 540 nm illumination. As illustrated, the MAPbI$_3$/SnO$_2$-2 PDs shows a decreased dark current and an improved photocurrent compared to MAPbI$_3$/SnO$_2$-1 PDs. According to previous reports,[17,40] the suppressed V$_O$ at the surface of SnO$_2$-2 thin films is responsible for the reduced dark current and improved photocurrent. Besides, the up-shift of conduction band of SnO$_2$-2 thin films further increases the photocurrent.[41] Fig. 5b shows the current–time curves of both
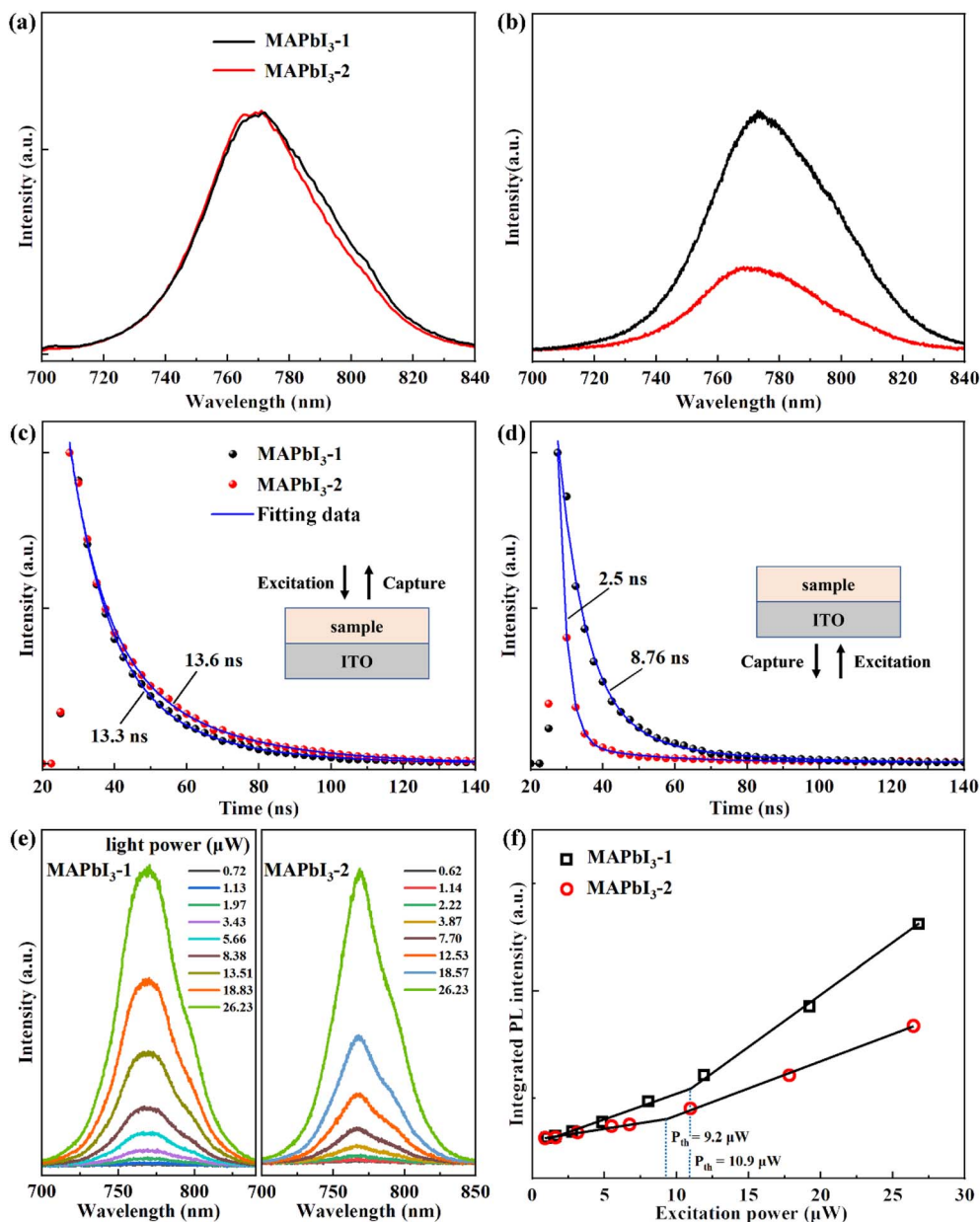
Fig. 3 Optical properties of $MAPbI_3$ thin films prepared on SnO_2-1 and SnO_2-2. (a and b) Steady-state and (c and d) transient PL spectra. (e and f) Excitation power dependent PL spectra. The PL data in a and c were captured from the front surface of $MAPbI_3$, as shown in Fig. 1c inset. The PL data in b, d, e and f were captured from the back surface of $MAPbI_3$, as shown in Fig. 1d inset.

PDs captured at zero bias with 540 nm illumination switched on and off. As shown, the photocurrent of both PDs increases linearly with an increase in light power, in which the slope of 0.06 A W^{-1} and 0.02 A W^{-1} for $MAPbI_3$/SnO_2-2 and $MAPbI_3$/SnO_2-1 PDs were derived (Fig. 5b inset). Generally, the increased slope of light power dependent photocurrent in $MAPbI_3$/SnO_2-2 PDs suggests the improved photodetection performance of them.

The photodetection performance of $MAPbI_3$/SnO_2 PDs was further evaluated from the responsivity and detectivity parameters. According to previous reports, the responsivity (R) and detectivity (D^*) were calculated using the following eqn (2) and (3):[17]

$$R = \frac{I_P - I_D}{P \times S} \quad (2)$$

$$D^* = \frac{R}{(2eI_D/S)^{0.5}} \quad (3)$$

where I_P and I_D are the photocurrent and dark current, S is the device area, P is the light power density (in W cm^{-2}), and e is the electron charge. Fig. 5c and d exhibit the responsivity and detectivity of $MAPbI_3$/SnO_2-1 and $MAPbI_3$/SnO_2-2 PDs at zero bias. As shown, both the PDs shows a good photodetection performance in the UV to vis spectral range (350 nm–750 nm). Notably, the $MAPbI_3$/SnO_2-2 PDs exhibits an improved responsivity and detectivity (0.077 A W^{-1} and 2×10^{11} jones), which
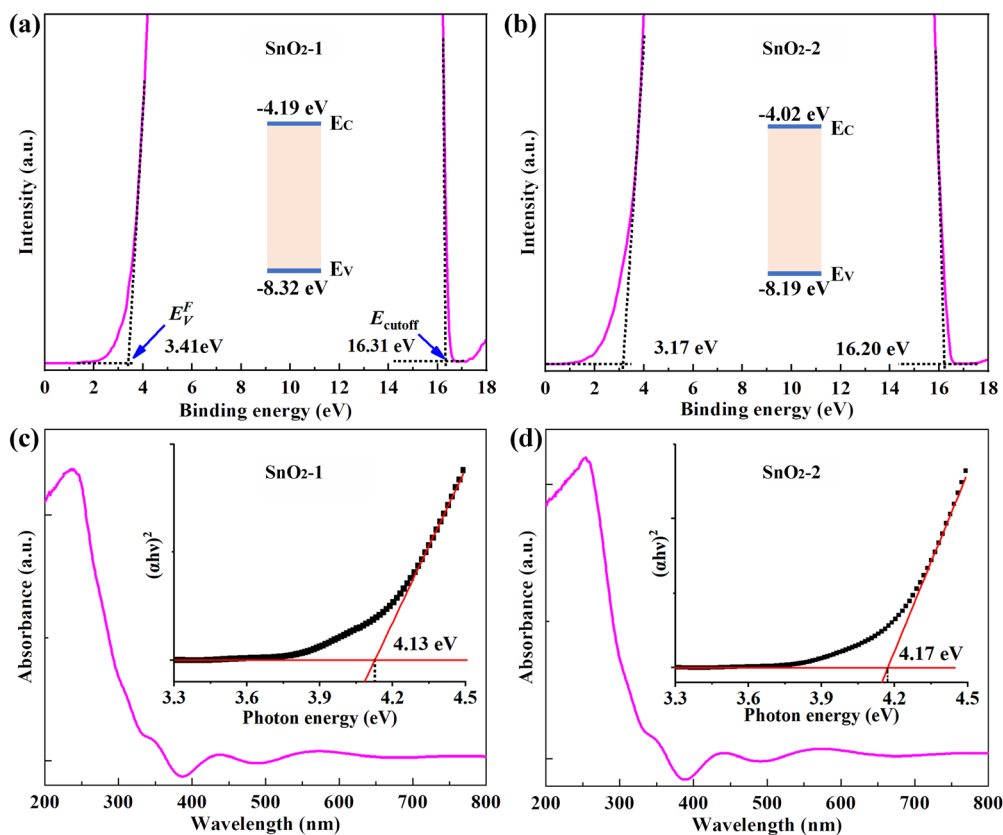
Fig. 4 (a and b) UPS and (c and d) absorption spectra of (a and c) SnO$_2$-1 and (b and d) SnO$_2$-2 thin films. The inset in (a and b) shows the energy band diagrams and in (c and d) shows the plot of $(\alpha h\nu)^2$ as a function of photon energy ($h\nu$).

are 2.5 times and 2 times higher than the MAPbI$_3$/SnO$_2$-1 PDs (0.03 A W^{-1} and 1 × 10^{11} jones). As discussed above, the improved photodetection performance is attributed to the modification of the buried SnO$_2$ thin films in terms of reduced surface V$_O$ and up-shift of conduction band. Meanwhile, a weak peak has appeared at around 850 nm in the responsivity and detectivity, which can be attributed to the defect-related absorption in the MAPbI$_3$ thin films.[42]

Finally, the mechanisms of improved photodetection performance in MAPbI$_3$/SnO$_2$-2 PDs are discussed. Fig. 6 illustrates the photodetection processes of MAPbI$_3$/SnO$_2$-1 and MAPbI$_3$/SnO$_2$-2 PDs. Initially, electron–hole pairs were generated within the MAPbI$_3$ thin films upon illumination. Then, the electrons were extracted by the SnO$_2$ thin films owing to the interfacial electrical field and the holes moved toward the Au electrode. As a result, remarkable photocurrent has been observed in the MAPbI$_3$/SnO$_2$-1 and MAPbI$_3$/SnO$_2$-2 PDs. However, remarkable non-radiative recombination occurred at the MAPbI$_3$/SnO$_2$-1 interface (Fig. 6a) due to the high density of V$_O$ at the surface of SnO$_2$-1 thin films. This resulted in an increased dark current and decreased photocurrent. In comparison, the non-radiative recombination was suppressed at the MAPbI$_3$/SnO$_2$-2 interface (Fig. 6b) owing to the suppressed V$_O$ at the surface of SnO$_2$-2. Accordingly, improved photocurrent and decreased dark current have been observed

simultaneously in the MAPbI$_3$/SnO$_2$-2 PDs. Besides, the up-shift of conduction band of SnO$_2$-2 facilitated the electron transport at the MAPbI$_3$/SnO$_2$ interface (Fig. 6b), which further improved the photocurrent. Collectively, the spin-coating procedure behaved a synergic effect including reduced surface V$_O$ and increased conduction band of the SnO$_2$, which accounted for the improved performance of photodetection of MAPbI$_3$/SnO$_2$-2 PDs.

In summary, performance-improved solution-processed MAPbI$_3$/SnO$_2$ heterojunction PDs have been fabricated by employing a stacked SnO$_2$ thin film prepared by sputtering and spin-coating methods in sequence. It has shown that the spin-coating procedure have little impacts on the growth of MAPbI$_3$ thin films, while it behaved a synergic effect such as reduced the surface V$_O$ and up-shifted the conduction band of SnO$_2$ thin films. The former suppressed the interfacial non-radiative recombination, while the latter aligned the energy-level at the MAPbI$_3$/SnO$_2$ interface and further improved the carrier transport. On these basis, the MAPbI$_3$/SnO$_2$ heterojunction PDs with a stacked SnO$_2$ thin film exhibited an improved photodetection performance in terms of reduced dark current and increased photocurrent, where an improved responsivity and detectivity of 0.077 A W^{-1} and 2.0 × 10^{11} jones, respectively, at the zero bias have been achieved. The results provided in this work provide a simple strategy for suppressing
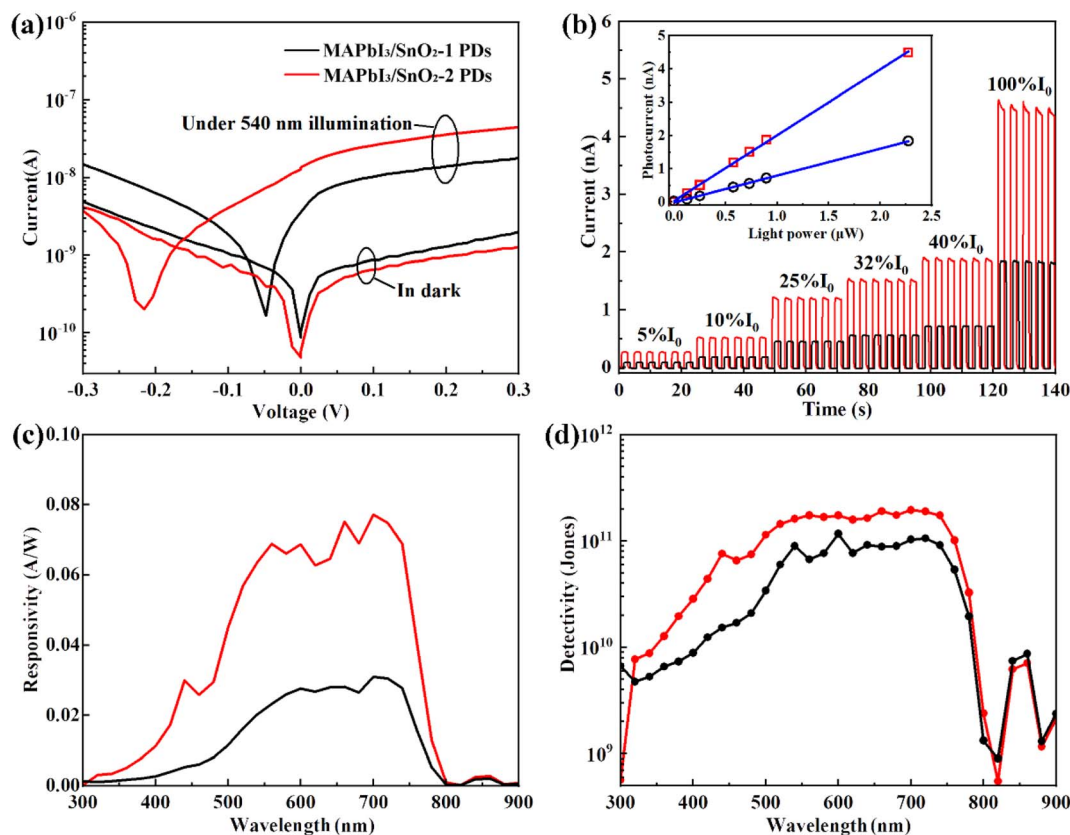
Fig. 5 Photodetection performance of MAPbI$_3$/SnO$_2$ PDs. (a) $I-V$. (b) Current−time curves. (c) Responsivity. (d) Detectivity. The bias in (b−d) is 0 V. The light was illuminated at the back surface of MAPbI$_3$ thin films.
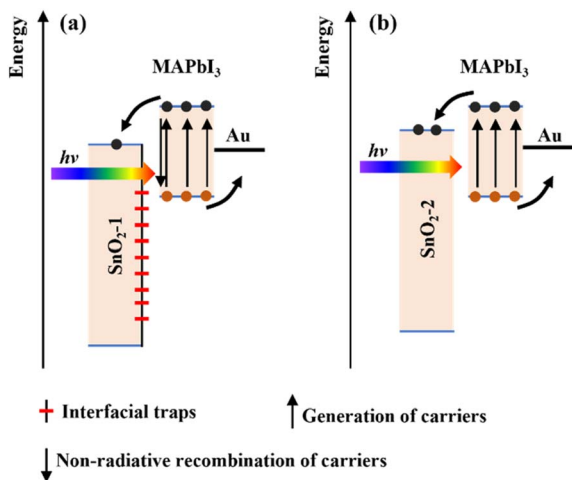

Fig. 6 Photodetection processes of (a) MAPbI$_3$/SnO$_2$-1 and (b) MAPbI$_3$/SnO$_2$-2 PDs.

the interfacial defects and aligning the energy-level simultaneously for improving the performance of perovskite heterojunction PDs in the future.

Data availability

The data that support the findings of this study are available from the corresponding authors upon reasonable request.

Conflicts of interest

The authors have declared that no conflict of interest exists.

References

1 L. Li, H. Chen, Z. Fang, X. Meng, C. Zuo, M. Lv, Y. Tian, Y. Fang, Z. Xiao, C. Shan, Z. Xiao, Z. Jin, G. Shen, L. Shen and L. Ding, An Electrically Modulated Single-Color/Dual-Color Imaging Photodetector, *Adv. Mater.*, 2020, **32**(24), 1907257.

2 W. Wu, X. Wang, X. Han, Z. Yang, G. Gao, Y. Zhang, J. Hu, Y. Tan, A. Pan and C. Pan, Flexible Photodetector Arrays Based on Patterned CH$_3$NH$_3$ PbI$_{(3-x)}$Cl$_{(x)}$ Perovskite Film for Real-Time Photosensing and Imaging, *Adv. Mater.*, 2019, **31**(3), 1805913.

3 P. Büchele, M. Richter, S. F. Tedde, G. J. Matt, G. N. Ankah, R. Fischer, M. Biele, W. Metzger, S. Lilliu, O. Bikondoa, J. E. Macdonald, C. J. Brabec, T. Kraus, U. Lemmer and O. Schmidt, X-ray imaging with scintillator-sensitized hybrid organic photodetectors, *Nat. Photonics*, 2015, **9**(12), 843–848.

4 C. Bao, J. Yang, S. Bai, W. Xu, Z. Yan, Q. Xu, J. Liu, W. Zhang and F. Gao, High Performance and Stable All-Inorganic Metal Halide Perovskite-Based Photodetectors for Optical Communication Applications, *Adv. Mater.*, 2018, **30**(38), 1803422.

5 J. Liu, M. Gao, J. Kim, Z. Zhou, D. S. Chung, H. Yin and L. Ye, Challenges and recent advances in photodiodes-based organic photodetectors, *Mater. Today*, 2021, **51**, 475–503.

6 Y. Yan, Q. Wu, Y. Zhao, S. Chen, S. Hu, J. Zhu, J. Huang and Z. Liang, Air-Stable and Self-Driven Perovskite Photodiodes with High On/Off Ratio and Swift Photoresponse, *Small*, 2018, **14**(41), 1802764.

7 M. V. Kovalenko, L. Protesescu and M. I. Bodnarchuk, Properties and potential optoelectronic applications of lead halide perovskite nanocrystals, *Science*, 2017, **358**(6364), 745–750.

8 L. K. Ono, Y. Qi and S. Liu, Progress toward Stable Lead Halide Perovskite Solar Cells, *Joule*, 2018, **2**(10), 1961–1990.

9 D. Nodari, L. J. F. Hart, O. J. Sandberg, F. Furlan, E. Angela, J. Panidi, Z. Qiao, M. A. McLachlan, P. R. F. Barnes, J. R. Durrant, A. Ardalan and N. Gasparini, Dark Current in Broadband Perovskite-Organic Heterojunction Photodetectors Controlled by Interfacial Energy Band Offset, *Adv. Mater.*, 2024, **36**(33), 2401206.

10 Y. Zhang, C. Li, E. Bi, T. Wang, P. Zhang, X. Yang and H. Chen, Efficient Inverted Perovskite Solar Cells with a Low-Dimensional Halide/Perovskite Heterostructure, *Adv. Energy Mater.*, 2022, **12**(48), 2202191.

11 J. Zhuang, J. Wang and F. Yan, Review on Chemical Stability of Lead Halide Perovskite Solar Cells, *Nano-Micro Lett.*, 2023, **15**(1), 84.

12 J. Zhou and J. Huang, Photodetectors Based on Organic-Inorganic Hybrid Lead Halide Perovskites, *Adv. Sci.*, 2018, **5**(1), 1700256.

13 L. Xiong, Y. Guo, J. Wen, H. Liu, G. Yang, P. Qin and G. Fang, Review on the Application of SnO_2 in Perovskite Solar Cells, *Adv. Funct. Mater.*, 2018, **28**(35), 1802757.

14 Q. Jiang, X. Zhang and J. You, SnO_2 : A Wonderful Electron Transport Layer for Perovskite Solar Cells, *Small*, 2018, 1801154.

15 C. Wu, B. Du, W. Luo, Y. Liu, T. Li, D. Wang, X. Guo, H. Ting, Z. Fang, S. Wang, Z. Chen, Y. Chen and L. Xiao, Highly Efficient and Stable Self-Powered Ultraviolet and Deep-Blue Photodetector Based on $Cs_2AgBiBr_6$/SnO_2 Heterojunction, *Adv. Opt. Mater.*, 2018, **6**(22), 1800811.

16 M. J. Paik, Y. Y. Kim, J. Kim, J. Park and S. I. Seok, Ultrafine SnO_2 colloids with enhanced interface quality for high-efficiency perovskite solar cells, *Joule*, 2024, **8**(7), 2073–2086.

17 P. Cheng, T. Zhao, M. Chen, S. Chen, X. Shen, Y. Liu, S. Yang, Z. Chen, X. Dong, Q. Wang and D. Cao, Improved Perovskite CH3NH3PbI3 Thin Films by ZIF-67 Additive Assisted Co Ion Doping toward High-Performance and Stable Photodetectors, *Adv. Opt. Mater.*, 2023, **11**(21), 2300757.

18 Y. Lin, Y. Bai, Y. Fang, Z. Chen, S. Yang, X. Zheng, S. Tang, Y. Liu, J. Zhao and J. Huang, Enhanced Thermal Stability in Perovskite Solar Cells by Assembling 2D/3D Stacking Structures, *J. Phys. Chem. Lett.*, 2018, **9**(3), 654–658.

19 Z. Yang, Y. Deng, X. Zhang, S. Wang, H. Chen, S. Yang, J. Khurgin, N. X. Fang, X. Zhang and R. Ma, High-Performance Single-Crystalline Perovskite Thin-Film Photodetector, *Adv. Mater.*, 2018, **30**(8), 1704333.

20 D. Yang, R. Yang, K. Wang, C. Wu, X. Zhu, J. Feng, X. Ren, G. Fang, S. Priya and S. F. Liu, High efficiency planar-type perovskite solar cells with negligible hysteresis using EDTA-complexed SnO_2, *Nat. Commun.*, 2018, **9**(1), 3239.

21 T. Bu, J. Li, F. Zheng, W. Chen, X. Wen, Z. Ku, Y. Peng, J. Zhong, Y. B. Cheng and F. Huang, Universal passivation strategy to slot-die printed SnO_2 for hysteresis-free efficient flexible perovskite solar module, *Nat. Commun.*, 2018, **9**(1), 4609.

22 W. Jang, Z. U. Rehman, M. Haris, J. S. Cho, J. Lim, M. S. Kim, J.-C. Lee, H. K. Lee and D. H. Wang, Oxide vacancy passivation through interface engineering of Tetraphenylethylene-Based Small-Molecule with sulfonate functional group for efficient organic photodetector, *Chem. Eng. J.*, 2023, **472**, 144847.

23 M. Sun, H. Zhang, C. Liang, C. Ji, X. Jing, F. Sun, Q. Song, F. You and Z. He, Exploring Electron Transporting Layer in Combination with a Polyelectrolyte for n–i–p Perovskite Solar Cells, *Adv. Mater. Interfaces*, 2020, **7**(17), 2000412.

24 M. Abuhelaiqa, N. Shibayama, X.-X. Gao, H. Kanda and M. K. Nazeeruddin, SnO2/TiO2 Electron Transporting Bilayers: A Route to Light Stable Perovskite Solar Cells, *ACS Appl. Energy Mater.*, 2021, **4**(4), 3424–3430.

25 Y. Zheng, J. Kong, D. Huang, W. Shi, L. McMillon-Brown, H. E. Katz, J. Yu and A. D. Taylor, Spray coating of the PCBM electron transport layer significantly improves the efficiency of p-i-n planar perovskite solar cells, *Nanoscale*, 2018, **10**(24), 11342–11348.

26 W. Xu, G. Lei, C. Tao, J. Zhang, X. Liu, X. Xu, W. Y. Lai, F. Gao and W. Huang, Precisely Controlling the Grain Sizes with an Ammonium Hypophosphite Additive for High-Performance Perovskite Solar Cells, *Adv. Funct. Mater.*, 2018, **28**(33), 1802320.

27 B. Li, C. Liu and X. Zhang, SnO_2-Based Interfacial Engineering towards Improved Perovskite Solar Cells, *Nanomaterials*, 2024, **14**(17), 14171406.

28 J. Jia, C. Qian, Y. Dong, Y. F. Li, H. Wang, M. Ghoussoub, K. T. Butler, A. Walsh and G. A. Ozin, Heterogeneous catalytic hydrogenation of CO_2 by metal oxides: defect engineering – perfecting imperfection, *Chem. Soc. Rev.*, 2017, **46**(15), 4631–4644.

29 J. Liu, S. Li, S. Liu, Y. Chu, T. Ye, C. Qiu, Z. Qiu, X. Wang, Y. Wang, Y. Su, Y. Hu, Y. Rong, A. Mei and H. Han, Oxygen Vacancy Management for High-Temperature Mesoporous SnO_2 Electron Transport Layers in Printable Perovskite Solar Cells, *Angew. Chem., Int. Ed.*, 2022, **61**(26), 202202012.

30 X. Wang, Y. Zhang, C. Zhou, D. Huo, R. Zhang and L. Wang, Hydroxyl-regulated BiOI nanosheets with a highly positive valence band maximum for improved visible-light photocatalytic performance, *Appl. Catal., B*, 2020, **268**, 118390.

31 J. H. Lee, D. Shin, R. Rhee, S. Yun, K. M. Yeom, D. H. Chun, S. Lee, D. Kim, Y. Yi, J. H. Noh and J. H. Park, Band Alignment Engineering between Planar SnO_2 and Halide Perovskites *via* Two-Step Annealing, *J. Phys. Chem. Lett.*, 2019, **10**(21), 6545–6550.

32 H. Min, D. Y. Lee, J. Kim, G. Kim, K. S. Lee, J. Kim, M. J. Paik, Y. K. Kim, K. S. Kim, M. G. Kim, T. J. Shin and S. Il Seok, Perovskite solar cells with atomically coherent interlayers on SnO$_2$ electrodes, *Nature*, 2021, **598**(7881), 444–450.

33 S. Zhang, H. Si, W. Fan, M. Shi, M. Li, C. Xu, Z. Zhang, Q. Liao, A. Sattar, Z. Kang and Y. Zhang, Graphdiyne: Bridging SnO$_2$ and Perovskite in Planar Solar Cells, *Angew. Chem., Int. Ed.*, 2020, **59**(28), 11573–11582.

34 H. Park, R. Chaurasiya, B. H. Jeong, P. Sakthivel and H. J. Park, Nickel Oxide for Perovskite Photovoltaic Cells, *Adv. Photonics Res.*, 2021, **2**(8), 2000178.

35 Y. Zhu, Q. Cui, J. Chen, F. Chen, Z. Shi, X. Zhao and C. Xu, Inhomogeneous Trap-State-Mediated Ultrafast Photocarrier Dynamics in CsPbBr$_3$ Microplates, *ACS Appl. Mater. Interfaces*, 2021, **13**(5), 6820–6829.

36 X. Shen, S. Yang, M. Chen, J. Su, J. Cai, P. Cheng, Y. Liu, Q. Wang and D. Cao, Interfacial Engineering with Aluminum Oxide toward an Improved Self-Powered Narrowband Visible-Light Photodetection in Lead Halide Perovskite CH$_3$NH$_3$PbBr$_3$/p-Si Heterojunctions, *Adv. Mater. Interfaces*, 2022, **9**(14), 2102305.

37 N. Wu, T. Yang, Z. Wang, Y. Wu, Y. Wang, C. Ma, H. Li, Y. Du, D. Zhao, S. Wang, P. Liu, W. Huang, X. Ren, S. F. Liu and K. Zhao, Stabilizing Precursor Solution and Controlling Crystallization Kinetics Simultaneously for High-Performance Perovskite Solar Cells, *Adv. Mater.*, 2023, **35**(44), 2304809.

38 J. C. Schuurman, A. R. McNeill, R. F. Martinez-Gazoni, J. I. Scott, R. J. Reeves, M. W. Allen and A. J. Downard, The effect of covalently bonded aryl layers on the band bending and electron density of SnO$_2$ surfaces probed by synchrotron X-ray photoelectron spectroscopy, *Phys. Chem. Chem. Phys.*, 2019, **21**(32), 17913–17922.

39 Y. Ai, W. Liu, C. Shou, J. Yan, N. Li, Z. Yang, W. Song, B. Yan, J. Sheng and J. Ye, SnO2 surface defects tuned by (NH4)2S for high-efficiency perovskite solar cells, *Sol. Energy*, 2019, **194**, 541–547.

40 L. Song, L. Huang, W. Xiao and J. Li, Improved performance and stability in CH$_3$NH$_3$PbI$_3$/Si heterojunction photodetectors realized by ZIF-67 additive assisted Co ion doping, *Appl. Phys. Lett.*, 2021, **118**(16), 033301.

41 E. H. Jung, B. Chen, K. Bertens, M. Vafaie, S. Teale, A. Proppe, Y. Hou, T. Zhu, C. Zheng and E. H. Sargent, Bifunctional Surface Engineering on SnO2 Reduces Energy Loss in Perovskite Solar Cells, *ACS Energy Lett.*, 2020, **5**(9), 2796–2801.

42 J. Wang, X. Duan and W. J. Yin, Photoinduced Dynamic Defects Responsible for the Giant, Reversible, and Bidirectional Light-Soaking Effect in Perovskite Solar Cells, *J. Phys. Chem. Lett.*, 2021, **12**(38), 9328–9335.